remote sensing

MDPI

Article

JPSS-4 VIIRS Pre-Launch Calibration Performance and Assessment

Amit Angal [1,*], David Moyer [2], Xiaoxiong Xiong [3], Daniel Link [1], Thomas Schwarting [1], Jeff McIntire [1], Qiang Ji [1] and Chengbo Sun [4]

[1] Science Systems and Applications Inc., 10210 Greenbelt Road, Lanham, MD 20706, USA
[2] The Aerospace Corporation, 2310 E. El Segundo Blvd., El Segundo, CA 90245, USA
[3] Sciences and Exploration Directorate, NASA Goddard Space Flight Center, Greenbelt, MD 20771, USA
[4] Global Science & Technology, Inc., 7501 Greenway Center Drive, Suite 1100, Greenbelt, MD 20770, USA
* Correspondence: amit.angal@ssaihq.com

Abstract

The Joint Polar Satellite System (JPSS) is a collaborative program between NASA and NOAA to provide scientific measurements from multiple polar-orbiting satellites. The development, testing, launch, and operation of the satellites is jointly overseen by NASA and NOAA, with NASA responsible for developing and building instruments, spacecraft, ground systems, and launching into orbit. While three VIIRS instruments are currently on-orbit, spacecraft integration of the two VIIRS instruments planned for launch on the JPSS-3 and -4 spacecraft is ongoing. The latest build in the series, set to be launched on the JPSS-4 platform, recently completed its main ground calibration program at the vendor facility. This program covered a comprehensive series of performance metrics designed to ensure that the instrument can maintain its calibration successfully on-orbit. In this paper, we present the results from the radiometric calibration process, which includes metrics such as dynamic range, signal-to-noise ratio, noise equivalent differential temperature, polarization sensitivity, scattered light response, relative spectral response, response versus scan angle, and crosstalk. All key metrics have met or exceeded their design requirements, with some minor exceptions. Also included are comparisons with previous VIIRS instruments, as well as a description of their expected performance once on-orbit.

Keywords: JPSS; VIIRS; RSB; TEB; pre-launch; EDR

check for updates

Academic Editor: Jorge Vazquez

Received: 1 May 2025
Revised: 13 June 2025
Accepted: 17 June 2025
Published: 23 June 2025

Citation: Angal, A.; Moyer, D.; Xiong, X.; Link, D.; Schwarting, T.; McIntire, J.; Ji, Q.; Sun, C. JPSS-4 VIIRS Pre-Launch Calibration Performance and Assessment. *Remote Sens.* **2025**, *17*, 2146. https://doi.org/10.3390/rs17132146

Copyright: © 2025 by the authors. Licensee MDPI, Basel, Switzerland. This article is an open access article distributed under the terms and conditions of the Creative Commons Attribution (CC BY) license (https://creativecommons.org/licenses/by/4.0/).

1. Introduction

The Visible Infrared Imaging Radiometer Suite (VIIRS) is an important sensor onboard the Suomi National Polar-orbiting Partnership (SNPP), NOAA-20 (formerly JPSS-1), and NOAA-21 (formerly JPSS-2) satellites, which are part of the Joint Polar Satellite Systems (JPSS) constellation [1]. VIIRS gathers global measurements of the atmospheric, terrestrial, and oceanic conditions, including sea and land surface temperatures, snow and ice cover, fire locations, water vapor, vegetation, etc. [2,3]. In addition to the continued generation of science products, some of these measurements also support the forecasting of severe weather, such as hurricanes, and assessing the impacts of environmental hazards, such as droughts, forest fires, and coastal water quality, etc. With the launch of two VIIRS instruments onboard the JPSS-4 and JPSS-3 satellites in 2027 and 2032, the JPSS constellation will provide continuity of global observations of the Earth's land, atmosphere, and oceans through 2038. The VIIRS instruments scheduled to be launched on the JPSS-4 and -3

spacecraft have completed their main ground test program at the RTX facility in El Segundo, CA, and are undergoing the observatory-level testing before launch. The radiometric calibration of the fifth VIIRS build (JPSS-4), based on its ground testing, is the focus of this paper.

To meet the stringent requirements of the scientific community, a well-calibrated VIIRS instrument is a prerequisite. To achieve this, the VIIRS instruments underwent a rigorous calibration program prior to launch, with the ground measurements having traceability to the NIST standards. RTX has successfully developed and implemented a comprehensive test program to calibrate the key aspects of the VIIRS instrument to ensure production of science-quality datasets. This paper will focus on the radiometric performance of the JPSS-4 VIIRS instrument based on the measurements collected during its ground testing. Although not a part of this work, it is worth noting that the test program also included and successfully performed a comprehensive geometric characterization of the JPSS-4 VIIRS instrument, with most metrics showing compliance with the specification. Section 2 will describe the instrument design, including an overview and timeline of the main test program and comparisons with the previous VIIRS builds. Section 3 will describe the sensor performance, including the radiometry, signal-to-noise ratio (SNR) or noise equivalent differential temperature (NEdT), polarization, response versus scan angle, scattered light, and relative spectral response.

2. JPSS-4 Sensor Design and Testing Program

2.1. Sensor Design

The VIIRS instrument follows the legacy of, and improves upon, the measurements that were made by the MODIS instruments onboard the Terra and Aqua platforms. VIIRS was designed to continue the long data record from the MODIS instruments, but with several key changes. Some of the changes incorporated in VIIRS include a consistent spatial resolution throughout the scan, high spatial resolution (375 m) thermal bands, and the inclusion of the day–night band (DNB), which allows for observations of light sources under varying conditions. The first VIIRS instrument was launched in October 2011 onboard the SNPP platform, followed by the November 2017 and November 2022 launches on the NOAA-20 and NOAA-21 platforms. The on-orbit performance of VIIRS has been documented extensively [4–6]. The pre-launch performance for the first four VIIRS builds has also been documented before [7–10].

The VIIRS design encompasses several advancements based on the lessons learned from the heritage sensors. The onboard calibrators (OBCs) include a solar diffuser (SD), SD stability monitor (SDSM), and onboard blackbody (BB). The combination of the rotating telescope assembly (RTA) and a half-angle mirror (HAM) is based on the SeaWiFS design to reduce the instrument response versus scan angle (RVS) effects and stray light contamination. VIIRS also incorporates dual gain bands, which use detector arrays that can switch between the high and low gain to enable an effective coverage of the dynamic range. Another design feature in VIIRS is the three-stage pixel aggregation, where the science data record (SDR) is generated using 3-to-1, 2-to-1, and 1-to-1 pixel aggregation from nadir to edge of the scan, which significantly reduces the pixel size growth with scan angle [2].

Figure 1 illustrates the VIIRS sensor design, consisting of two modules that are separately mounted to the spacecraft: the optomechanical module (OMM) and the electronics module (EM). The OMM consists of all the optical and mechanical assemblies required to collect the Earth and calibration data, whereas the EM provides all the electrical interfaces to the spacecraft to command and control the VIIRS configuration. The VIIRS telescope scans the space view (SV), the Earth, the BB, and the SD sequentially. The rotating telescope scans the Earth's surface, which is reflected from the HAM into the aft-optics subsystem.

The two dichroic beam splitters direct the incoming light onto four different focal plane arrays: the visible and near infrared (VISNIR), the short-wave and mid-wave infrared (SMIR), the long-wave infrared (LWIR), and the DNB focal plane assemblies (FPAs).

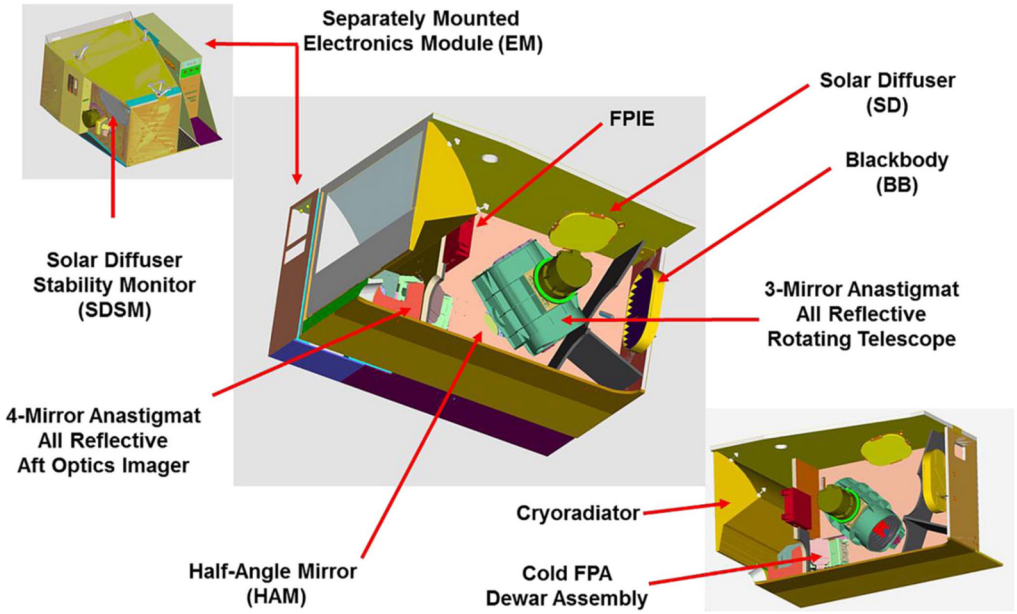


Figure 1. VIIRS sensor design based on two separate modules—EM and OMM—which include the RTA, HAM, and aft-optics.

Each moderate resolution or imaging band is a linear array of 16 or 32 detectors aligned in the direction of the spacecraft's motion. The imaging bands (names beginning with "I") have resolutions of 375 m at nadir, while the moderate-resolution bands (names beginning with "M") have resolutions of 750 m at nadir. Some bands have two gain states (high and low gain, or HG and LG). VIIRS has a total of 14 reflective solar bands (RSBs), seven M-bands (M1–M7) and two I-bands (I1 and I2) located on the VISNIR FPA, and four M-bands (M8–M11) and one I-band (I3) located on the SMIR FPA. Out of these bands, M1–M5 and M7 are dual gain bands. The RSBs have a spectral coverage from 0.4 to 2.25 μm. In addition, VIIRS has seven thermal emissive bands (TEBs) located on two separate FPAs: two M-bands (M12 and M13) and one I-band (I4) on the SMIR FPA and three M-bands (M14–M16) and one I-band (I5) on the LWIR FPA. The mid-wave infrared (MWIR) bands cover the spectrum between 3.7 μm to 4.1 μm, whereas the LWIR bands cover the spectrum between 8.55 to 12 μm. For the M16 band, there are two sets of 16 detectors, known as M16A and M16B. The M16 band data is the time delay integration of M16A and M16B. Table 1 provides per-band information, which includes the ground field-of-view, spectral range, typical radiance (DNB, VNIR, and SWIR focal planes) or temperature (MWIR and LWIR focal planes) for each gain stage of the band, maximum radiance or temperature, and signal-to-noise ratio or noise-equivalent-delta temperature. The DNB utilizes a temperature-controlled CCD with multiple gain stages (LGS, MGS, HGA, and HGB) to cover a wide dynamic range and capture both day and night imagery. The high-gain stages (HGA and HGB) are redundant and operate in time delay integration (TDI) to improve signal-to-noise ratio, particularly during nighttime observations. The DNB employs on-board aggregation to maintain a 750 m spatial resolution across the entire swath and uses 32 aggregation modes.

The SD is a Spectralon® diffuser with its bidirectional reflectance distribution function (BRDF) measured pre-launch. Together with an SD attenuation screen, it acts as a primary calibration source for the VIIRS RSB. To track the on-orbit change of the SD's BRDF, a solar diffuser stability monitor (SDSM), a stand-alone instrument with eight silicon detectors

equipped with filters to match the VISNIR bandpasses, is used to measure the direct sun view and the SD view in a near-simultaneous manner. A full-aperture BB with a V-groove design and six thermistors serves as the primary calibration source for the TEB. During nominal operations, the BB is controlled at 292.5 K but can be commanded from ambient to 315 K.

Table 1. VIIRS band design information that includes the ground field-of-view, spectral range, typical radiance (DNB, VNIR, and SWIR bands) or temperature (MWIR and LWIR bands) for each gain stage of the band, maximum radiance or temperature, and signal-to-noise ratio or noise-equivalent-delta temperature. Radiances in $W/m^2/Sr/\mu m$ and temperature in Kelvin. Note: The DNB specification is for L_{min}, where the SNR requirement is evaluated. There is no L_{typ} specified for DNB.

Band	Ground FOV (m)	Spectral Range (μm)	Gain Stage	L_{typ} or T_{typ}	L_{max} or T_{max}	SNR or NEdT
			VNIR			
DNB	750	0.50–0.90	Variable	0.00003	200	6
M1	750	0.40–0.42	High	44.9	135	352
			Low	155	615	316
M2	750	0.43–0.45	High	40	127	380
			Low	146	687	409
M3	750	0.47–0.49	High	32	107	416
			Low	123	702	414
M4	750	0.54–0.56	High	21	78	362
			Low	90	667	315
I1	375	0.6–0.68	Single	22	718	119
M5	750	0.66–0.68	High	10	59	242
			Low	68	651	360
M6	750	0.73–0.75	Single	9.6	41	199
I2	375	0.84–0.88	Single	25	349	150
M7	750	0.84–0.88	High	6.4	29	215
			Low	33.4	349	340
			SWIR			
M8	750	1.23–1.25	Single	5.4	165	74
M9	750	1.37–1.38	Single	6	77.1	83
I3	375	1.58–1.64	Single	7.3	72.5	6
M10	750	1.58–1.64	Single	7.3	71.2	342
M11	750	2.22–2.27	Single	0.12	31.8	10
			MWIR			
M12	750	3.66–3.84	Single	270	353	0.396
M13	750	3.97–4.12	High	300	343	0.107
			Low	380	634	0.423
I4	375	3.55–3.93	Single	270	353	2.5
			LWIR			
M14	750	8.40–8.70	Single	270	336	0.091
M15	750	10.26–11.26	Single	300	343	0.07
I5	375	10.50–12.40	Single	210	340	1.5
M16	750	11.53–12.48	Single	300	340	0.072

While there have not been any significant changes in the VIIRS design, there have been some component-level modifications between builds that have affected the performance and compliance. Several improvements were made to JPSS-3 based on the lessons learned from JPSS-2 VIIRS characterization. These included a DNB CCD with updated biases, improved dichroic to reduce polarization sensitivity, SDSM filter redesign to reduce out-of-band leaks, tighter RTA tolerancing for wavefront error and line-of-sight, and tighter effective focal length bounds to achieve scan overlap. During the later stages of the JPSS-3 TVAC testing, the single-layer insulation seam tape was observed to short the cryoradiator's cold stage to the intermediate stage, leading to a loss of thermal margin, a behavior that could have had a significant impact on the performance post-launch. This issue was addressed in JPSS-3 VIIRS and in JPSS-4 VIIRS, as both builds have the same design. A few other modifications related to parts, materials, and processes were also incorporated, but are not expected to have any impact on the VIIRS performance post-launch.

2.2. Sensor Testing Program

The VIIRS instrument, scheduled to be launched on the JPSS-4 spacecraft, completed its intensive ground test program to ensure proper instrument characterization and calibration. Since the testing on VIIRS Flight Unit 1 (F1), launched later on the SNPP spacecraft, the program has undergone certain modifications and enhancements based on the lessons learned from the testing of each build. The VIIRS test program covers the following pre-launch phases: sensor ambient (Fall 2021), pre-thermal vacuum (TV), sensor TV, sensor post-TVAC (August to December 2023), and spacecraft TV (expected in 2026).

During the ambient phase of testing, several key characterizations are performed, including the instrument polarization sensitivity, response-versus-scan angle (RVS), near-field response (NFR), stray light, preliminary gain characterization, and, most importantly, the relative spectral response characterization (RSR) using laser-based measurements from the Goddard Laser-based Absolute Measurement of Radiance (GLAMR) system [11]. The key sensor characteristics that were observed from these tests are discussed in this paper. The TVAC phase of testing provides the key characterization of the instrument gain at three different temperature plateaus, as well as the sensitivity of the gain in relation to changing EM and OMM temperatures during each transition. These measurements form the basis of the look-up tables (LUTs) that are derived for on-orbit calibration. Furthermore, various performance metrics, such as SNR, dynamic range, saturation, radiometric response uniformity, and radiometric characterization uncertainty, are also evaluated from this dataset. The Spectral Measurement Assembly (SpMA)-based measurements acquired during the TVAC testing combined with the GLAMR-based measurements culminated in an at-launch release version of the relative spectral response [12]. TVAC testing measured the dynamic range, noise, and gain transition, but also characterized the detector response at three temperature plateaus: cold (~253 K), nominal (~268 K), and hot (~283 K). JPSS-4 VIIRS demonstrated the expected functionality and performance at a cold focal plane assembly (CFPA) set point of 80 K during TVAC testing. The instrument will be operated at this CFPA set point at launch.

3. JPSS-4 Pre-Launch Characterization and Performance

This section will review the pre-launch characterization and performance of the JPSS-4 VIIRS instrument.

3.1. RSB Calibration Performance

The RSB calibration is performed using a NIST-traceable 100 cm-diameter spherical integration source (SIS-100) and a high-radiance three-mirror collimator (TMC) SIS for the

short wavelength low gain bands where the SIS-100 does not sufficiently cover the dynamic range. Also included as part of the test setup is a linear attenuator assembly (LAA), which consists of a metal sheet with evenly spaced holes designed to provide a transmission of approximately 56% [13]. The screen is mounted on a linear drive to move it in and out of the optical path of the source. Since the RSB sources are not known to the accuracy necessary for a direct radiance versus *dn* polynomial fit, the dn_{out} and dn_{in}, in pairs, are used to compute the shape of the calibration curve. Equation (1) presents the polynomial relationship of the VIIRS response to the SIS without the LAA in the optical path dn_{out} in terms of calibration coefficients: c_0, c_1, and c_2:

$$L_{SIS} = c_0 + c_1 dn_{out} + c_2 dn_{out}^2 \quad (1)$$

Equation (2) similarly relates the VIIRS response to the SIS with LAA attenuation (dn_{in}) to the same coefficients. This requires an additional term to account for the signal attenuation (τ_{LAA}):

$$L_{SIS} = \frac{c_0 + c_1 dn_{in} + c_2 dn_{in}^2}{\tau_{LAA}} \quad (2)$$

The SIS is cycled through a series of illumination levels in both fixed high gain and fixed low gain to ensure coverage across the entire dynamic range. Figure 2 (left panel) shows an example of VIIRS response (*dn*) versus the SIS-100 radiance (L) for the high-gain stage of band M2. Using the least squares fit, the calibration coefficients are estimated. The middle panel shows the fractional fit residuals, and the right panel depicts the measured SNR showing compliance against specification. The dn_{in} and dn_{out} for each SIS-100 source level are used in a least squares regression to determine the τ_{LAA}, $(\frac{c_0}{c_1})$, and $(\frac{c_2}{c_1})$ values for each gain state, band, detector subframe, and HAM side. These calibration coefficients are then included as a part of the at-launch LUT that is used for on-orbit SDR generation. In most cases, the $(\frac{c_0}{c_1})$ term was very small and will likely be set to zero in the on-orbit calibration, as has been the case in the current VIIRS instruments. The term $(\frac{c_2}{c_1})$ was also seen to be extremely small (on the order of 10^{-6}), with no major detector dependence observed. One exception to this behavior is the larger $(\frac{c_0}{c_1})$ in the case of band I3, indicating some non-linearity at the lower end of the dynamic range. Such behavior was more widespread in all the SWIR bands on JPSS-1 VIIRS and was addressed on-orbit via a quartic calibration expression, an approach that could also be adopted for JPSS-4 VIIRS.

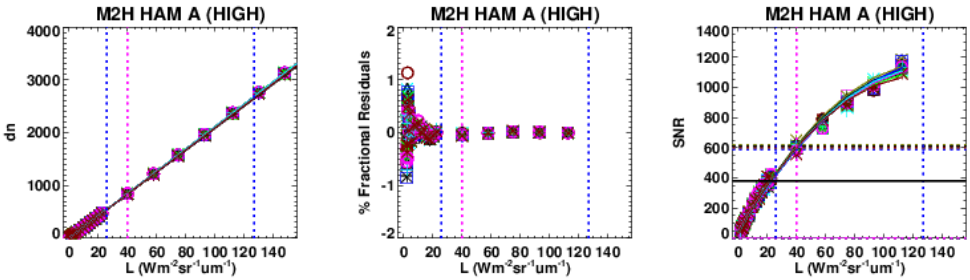


Figure 2. (**Left**) VIIRS response for each detector (different color) plotted versus SIS-100 L for band M2 from nominal plateau performance testing. Blue vertical dotted lines denote L_{min} and L_{max}; the pink line denotes L_{typ}. (**Middle**) Fractional residuals associated with the fits shown in the left panel. (**Right**) SNR plotted versus SIS-100 radiance and evaluated (horizontal dotted lines) against the specification (solid black horizontal line) at L_{typ}.

In addition to the radiometric gains, the SNR was also measured as a function of radiance using the SIS-100 data collected. A model was used to fit the measured SNR to estimate the value at a typical radiance, which is compared with the specification. Shown in Table 2 are the band-averaged SNR values for all builds from the nominal plateau data

collected, showing compliance by large margins. For ease of presenting the results, the JPSS 1–4 VIIRS are referred to as J1 to J4 in the result tables. The dynamic range of the RSBs is assessed by comparing the saturation radiance with the maximum radiance (also listed in Table 1). The measured band average saturation radiances for all VIIRS builds are included in Table 3. All bands on JPSS-4 saturate above L_{max}. In previous builds (SNPP through JPSS-2 VIIRS), bands I3 and M8 saturated early (below Lmax). Digital saturation was observed for bands M2-M7, M9-M11, and I1 (analog saturation was observed for bands M4-M7 and M9-M10 at a radiance above the digital saturation); analog saturation was also observed for bands M8, I2, and I3. Due to hardware improvements in J2 onwards, the rollover behavior for most bands is observed at larger radiance values compared to SNPP and J1. This is expected to decrease the number of pixels impacted by rollover in the SDRs on-orbit. In the case of the dual gain bands, the data collected during the radiometric testing was also used to assess whether the bands met the transitional radiance requirements.

Table 2. Pre-launch SNR results from the nominal plateau, collected for all VIIRS builds.

Band	Gain	SNR_Spec	SNPP	J1	J2	J3	J4
M1	HG	352	613	636	650	680	679
M1	LG	316	1042	1066	1040	1038	1108
M2	HG	380	600	573	600	616	602
M2	LG	409	963	986	1040	1017	1023
M3	HG	416	683	706	753	764	755
M3	LG	414	1008	1063	1240	1140	1095
M4	HG	362	526	559	611	601	596
M4	LG	315	864	844	993	907	985
M5	HG	242	373	380	366	353	354
M5	LG	360	776	751	730	759	761
M6	HG	199	409	428	429	399	412
M7	HG	215	524	549	564	530	533
M7	LG	340	721	760	950	814	1064
M8	HG	74	358	335	240	364	279
M9	HG	83	290	325	232	204	212
M10	HG	342	691	765	685	662	537
M11	HG	10	105	216	198	223	217
I1	HG	119	261	227	212	235	276
I2	HG	150	273	287	285	266	277
I3	HG	6	176	190	172	180	147

During the temperature transition between the plateaus, the SIS-100 at a fixed illumination level is used to assess the stability of the calibration coefficients with varying temperatures. These measurements will supplement the calibration coefficients computed at each plateau while preparing the at-launch LUTs. Furthermore, the SIS-100 at a fixed illumination level was also used to assess temporal stability and stability with respect to varying bus voltages. A design requirement limits the variability of the gain between two successive calibrations to be less than 0.3%, where the two successive calibrations correspond to two SD views on orbit, separated by about 100 min. The variations for all

RSB with respect to the temporal or bus voltage changes were very small, well within the 0.3% requirement. More details on the JPSS-4 VIIRS RSB can be found here [14].

Table 3. Pre-launch saturation radiance trending from the nominal plateau, collected for all VIIRS builds. The L_{sat} and L_{max} values are in $W/m^2/sr/um$.

Band	Gain	L_{max} (Spec)	L_{sat}				
			SNPP	J1	J2	J3	J4
M1	HG	135	172	154	184	170	172
M1	LG	615	696	705	674	690	670
M2	HG	127	138	137	156	152	161
M2	LG	687	827	880	860	830	824
M3	HG	107	125	113	114	115	119
M3	LG	702	843	838	908	884	850
M4	HG	78	88	87	87	90	91
M4	LG	667	872	851	771	713	722
M5	HG	59	66	61	68	71	73
M5	LG	651	726	725	910	866	879
M6	HG	41	48	48	50	50	52
M7	HG	29	31	31	33	34	35
M7	LG	349	414	409	400	392	396
M8	HG	164.9	126	118	167	170	191
M9	HG	77.1	84	80	92	119	100
M10	HG	71.2	81	77	96	89	105
M11	HG	31.8	35	35	35	39	36
I1	HG	718	771	777	930	910	925
I2	HG	349	413	410	444	468	446
I3	HG	72.5	70	66	101	89	101

3.2. TEB Calibration Performance

The VIIRS TEB calibration is referenced to the blackbody calibration source (BCS), a NIST traceable source, with uncertainty less than 0.06 K at 10 μm and 300 K. Other blackbody sources included in the pre-launch testing were the high temperature blackbody and the three-mirror collimator (TMC) blackbody, placed outside of the TVAC chamber, with a maximum temperature of about 760 K, and required to calibrate the M13 low gain. The remaining two sources included the onboard blackbody, which provides calibration post-launch, and a cold BB source maintained at around ~90 K to simulate the deep space view required for background subtraction.

During the performance testing at the three temperature plateaus, the sources were cycled through a series of discrete temperature levels, whereas the source temperatures are fixed during the stability testing. Results from performance testing were used to assess various metrics such as NEdT, the absolute radiometric difference (ARD), the radiometric characterization uncertainty, and the radiometric response uniformity. In addition to the performance testing at the CFPA baseline temperature of 80 K, there were additional special and limited tests where the BB temperature was cycled for CFPA set points of 78 K and 82 K. Testing at additional CFPA temperatures leads to a more complete characterization

of the VIIRS TEB and acts as a contingency for scenarios where an alternate CFPA set point is preferred. This proved useful for J2 VIIRS when the CFPA temperature on-orbit was changed from the baseline pre-launch temperature of 82 K to 80 K due to better-than-expected cryocooler performance. The CFPA set point chosen during preflight testing has varied over the different VIIRS builds, with 80 K in the case of SNPP, 80.5 K for J1, 82 K for J2 and J3, and 80 K for J4.

The TEB radiometric calibration assumes the radiance reaching a given detector is the sum of the source radiance and contributors along the optical path (i.e., the RTA, HAM, and aft optics). The path difference radiance between the two sources (BCS and SV) is calculated as:

$$\Delta L_{BCS} = RVS_{BCS}\varepsilon_{BCS}L_{BCS} - \frac{(RVS_{BCS} - RVS_{SV})}{\rho_{RTA}}[L_{HAM} - (1-\rho_{RTA})L_{RTA}] \quad (3)$$

where RVS is the scan angle-dependent relative reflectance of the HAM, and the reflectance factors represent the total reflectance of the RTA mirrors. The temperature of each source is determined from one or more thermistors and the radiances for the sources are determined via Planck's law, convolved over the J4 VIIRS RSR for each spectral band. The path difference radiance is modeled as a quadratic polynomial as follows:

$$\Delta L = c_0 + c_1 dn + c_2 dn^2 \quad (4)$$

where dn represents the offset corrected digital response. Finally, the retrieved Earth view (EV) radiance for the BCS is determined by inverting Equation (3), expressed as:

$$L_{BCS-ret} = \frac{(c_0 + c_1 dn_{BCS} + c_2 dn_{BCS}^2)}{RVS_{BCS}} + \frac{(RVS_{BCS} - RVS_{SV})}{RVS_{BCS}\rho_{RTA}}[L_{HAM} - (1-\rho_{RTA})L_{RTA}] \quad (5)$$

TEB radiometric calibration coefficients were calculated for all detectors, HAM sides, electronic sides, temperature plateaus, and CFPA set points where testing was performed. NEdT is a metric to quantify the variation in the scene temperature equivalent to the system noise and was computed using the inverse of Planck's law with respect to source temperature. SNR was modeled as a path difference source radiance divided by the square root of a quadratic polynomial.

Figure 3 shows an example of the response and NEdT trends for the detectors of I5 HAM A, subsample (SS) one, electronic side A from the nominal plateau measurements. In general, the offset coefficients (c_0) are on the order of 10^{-2} or less and show consistent behavior over instrument conditions and electronic sides. The LWIR offset term exhibited detector dependence but not TV plateau dependence, except M14, which showed some sensitivity to instrument temperature. The non-linear coefficients (c_2) were generally small, with values less than 10^{-8}. The band average gains ($1/c_1$) were computed for all TV test instrument configurations. The MWIR gains showed small changes (<2%) as a function of the CFPA set point, and the LWIR gains showed 5–10% increases as the temperature increased, a behavior that is consistent with previous VIIRS builds. The gain temperature sensitivities are used to create the on-orbit calibration coefficient LUTs that adjust for the different instrument temperatures. Separate LUTs are made for each CFPA temperature set point and electronics side configuration. The instrument stability was tested as a function of time (at each plateau), temperature (during the transitions between the plateaus), and with respect to bus voltages to simulate expected on-orbit variations. Together with the gain temperature sensitivities, the temperature dependence during the plateau transitions is also used in the generation of the on-orbit calibration coefficient LUTs.

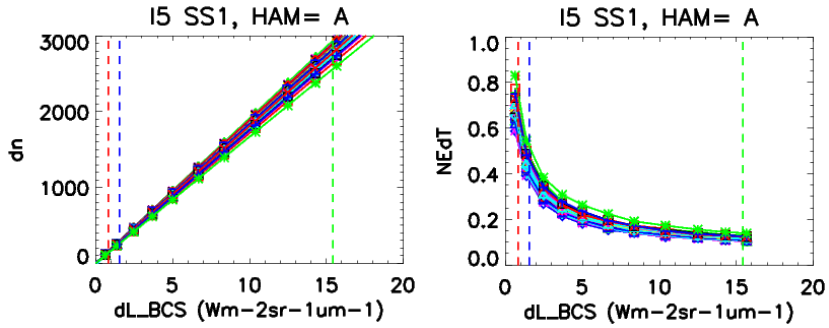


Figure 3. (**Left**) dn versus L trends for the I5 detectors from the nominal plateau collections. (**Right**) NEdT plotted as a function of BCS temperatures. The vertical dashed lines denote the L_{min}, L_{typ}, and L_{max}, respectively.

As shown in Figure 3, the NEdT increases as the scene temperature decreases. In the case of LWIR bands, the NEdT is below 0.5 K at even low scene temperatures, but for the MWIR bands, it increases between 3–6 K at 230 K, an expected behavior that was also observed in previous builds. The instrument requirement on the NEdT at the typical scene temperature along with the measured values for primary electronic side at the chosen CFPA set point are shown in Table 4. There is only a slight increase in the NEdT at T_{typ} with the CFPA temperature for the LWIR bands, but it does show a slight increase with the instrument temperature for all bands on both electronic sides. Also listed in Table 4 is the specification and the values from previous builds, which show compliance by a significant margin.

Table 4. NEdT performance in K for J4 VIIRS compared with previous VIIRS builds. The values presented are band-averaged for the primary electronic side and the chosen (at launch) CFPA set point.

Band	Gain	Ttyp	Spec	SNPP	J1	J2	J3	J4
M12	HG	270	0.396	0.130	0.119	0.150	0.129	0.123
M13	HG	300	0.107	0.044	0.044	0.047	0.046	0.048
M13	LG	380	0.423	0.340	0.236	0.231	0.219	0.258
M14	HG	270	0.091	0.061	0.053	0.055	0.053	0.040
M15	HG	300	0.07	0.030	0.027	0.036	0.027	0.029
M16A	HG	300	0.072	0.038	0.043	0.038	0.044	0.034
M16B	HG	300	0.072	0.038	0.044	0.037	0.043	0.032
I4	HG	270	2.5	0.410	0.393	0.400	0.344	0.312
I5	HG	210	1.5	0.420	0.423	0.403	0.502	0.427

The dynamic range is defined, at the low end, by an SNR limit of 3, and on the high end, by the saturation, as shown in Table 5. All bands saturate above the specified maximum temperature, with all bands except I4 and M12 saturating digitally first. These two bands exhibit analog saturation at higher radiance, a behavior common to all VIIRS builds, which leads to a rollover in the response, resulting in false lower radiance values showing up for some pixels. The small percentage of pixels affected by this behavior have been successfully flagged in the science products and can also be correlated with M13 to obtain any critical scientific information that might be compromised. Additional measurements were made for J3 and J4 to characterize the rollover region for use in fire detection algorithms.

Table 5. Saturation temperature in K for J4 VIIRS compared with previous VIIRS builds. The values presented are for the primary electronic side and the chosen (at launch) CFPA set point.

Band	Gain	Ttyp	Tmax	SNPP	J1	J2	J3	J4
M12	HG	270	353	357	359	360	361	361
M13	HG	300	343	364	363	363	366	366
M14	HG	270	336	347	348	352	363	353
M15	HG	300	343	365	357	350	360	360
M16A	HG	300	340	368	366	356	363	357
M16B	HG	300	340	368	367	353	364	357
I4	HG	270	353	357	357	355	360	357
I5	HG	210	340	373	369	380	381	368

The low gain of M13 was observed to digitally saturate only during the ambient testing in the case of J3 and J4 and, hence, is not included here. For the low end of the dynamic range, the SNR was observed to be over 100 for the bands M15, M16A, and M16B, and was between 10 and 50 for bands I5, M12, and M13, but reduced to below 3 (threshold) inside the specified dynamic range for I4 and M14. This is largely attributed to the larger noise in I4 (compared with M12) and the large difference in the RVS from space view to Earth view in the case of M14.

The ARD specification denotes the percentage difference between the calculated retrieved radiance and theoretical scene radiance based on source temperature measurements and is shown in Table 6 for all VIIRS builds at the specified temperatures. The ARD are largely consistent over all temperature conditions (instrument and CFPA) as well as electronic sides. While the ARD for all LWIR bands is less than 0.2% above 210 K, the MWIR bands I4, M12, and M13 have an ARD up to 0.8% for scene temperatures above 270 K, indicating the fitting inaccuracy to the radiance retrieval for these bands.

Table 6. VIIRS TEB ARD in (%) relative to sensor specification.

	Sensor	I4	I5	M12	M13	M14	M15	M16A	M16B
190	Spec	~	~	~	~	12.30	2.10	1.60	1.60
	NPP					1.72	0.53	0.23	0.25
	J1	~	~	~	~	1.48	0.18	0.15	0.15
	J2	~	~	~	~	0.68	0.29	0.17	0.25
	J3	~	~	~	~	2.97	0.40	0.23	0.24
	J4	~	~	~	~				
230	Spec	~	~	7.00	5.70	2.40	0.60	0.60	0.60
	NPP			1.8	3.43	0.18	0.08	0.03	0.04
	J1	~	~	0.34	1.50	0.15	0.05	0.00	0.01
	J2	~	~	7.60	2.95	0.11	0.07	0.08	0.04
	J3	~	~	2.63	0.80	0.34	0.04	0.06	0.09
	J4	~	~	2.59	2.95	0.18	0.1	0.1	0.09

Table 6. *Cont.*

	Sensor	I4	I5	M12	M13	M14	M15	M16A	M16B
267	Spec	5.00	2.50	~	~	~	~	~	~
	NPP	0.58	0.05						
	J1	0.45	0.02	~	~	~	~	~	~
	J2	0.48	0.10	~	~	~	~	~	~
	J3	0.69	0.06	~	~	~	~	~	~
	J4	0.43	0.08	~	~	~	~	~	~
270	Spec	~	~	0.70	0.70	0.60	0.40	0.40	0.40
	NPP			0.33	0.45	0.04	0.05	0.02	0.02
	J1	~	~	0.21	0.31	0.10	0.08	0.02	0.03
	J2	~	~	0.24	0.15	0.08	0.05	0.04	0.04
	J3	~	~	0.42	0.48	0.18	0.08	0.06	0.08
	J4	~	~	0.24	0.30	0.14	0.07	0.02	0.03
310	Spec	~	~	0.70	0.70	0.40	0.40	0.40	0.40
	NPP			0.31	0.38	0.09	0.02	0.02	0.03
	J1	~	~	0.31	0.35	0.16	0.09	0.05	0.05
	J2	~	~	0.25	0.17	0.11	0.06	0.03	0.04
	J3	~	~	0.48	0.35	0.27	0.12	0.08	0.09
	J4	~	~	0.31	0.21	0.20	0.07	0.04	0.06
340	Spec	~	~	0.70	0.70	0.50	0.40	0.40	0.40
	NPP			0.31	0.39	0.06	0.04	0.02	0.01
	J1	~	~	0.30	0.39	0.17	0.08	0.02	0.04
	J2	~	~	0.27	0.18	0.09	0.05	0.03	0.03
	J3	~	~	0.40	0.31	0.26	0.11	0.10	0.10
	J4	~	~	0.21	0.24	0.18	0.08	0.05	0.06

Another metric used to diagnose possible detector-to-detector striping is the radiance response uniformity (RRU), which is measured by comparing the difference of the retrieved radiance per detector with the average of the measured NEdL, with a value of 1, indicating a potential for striping. As in previous builds, this metric was seen to increase with temperatures but met the design requirement that applies between L_{min} and 0.9 L_{max} for all bands except M12 at the highest scene temperature. Similar to the RSBs, the TEB calibration stability is also characterized at a fixed BCS temperature while varying the instrument conditions. The temporal and bus voltage variations were very small, with maximums of about 0.2%. For the instrument temperature, the variation with analog signal processor and OMM temperatures was measured to be about 0.4% for the LWIR bands and less than 0.2% for the MWIR bands. The gain and noise performance of the LWIR bands varies significantly with FPA temperature, and this influences the dynamic range when testing at different FPA set points. More details on the JPSS-4 VIIRS TEB can be found here [15].

3.3. DNB Calibration Performance

The DNB radiometric calibration process requires two offset tables, one applied in the flight software and the second applied in the ground calibration, and a linear gain coefficient. In addition, an important aspect of the DNB calibration is the assessment of

the stray light when the satellite passes through the penumbra. As a part of the dark offset characterization test, data is collected in the dark conditions to measure the offsets and compute the onboard table, and then a repeat run with the onboard tables uploaded to characterize the remaining offset is performed to prepare a corresponding table for ground calibration. The tables are designed to flat-field the DNB and are set at target values of 350 for HGA and HGB, 200 for MGS, and 60 for LGS in 14-bit DN. The at-launch tables were produced from the nominal plateau measurements with all samples in each of the CCDs reaching the target level. Some values of the onboard offsets for samples in HGB on the A-side (and B-side) electronics were larger than 5% of the dynamic range, which required an adjustment to the saturation threshold, a process that was also necessary for J3 VIIRS.

As with the RSB, the radiometric test measures the DNB response of the SIS calibrated light levels to estimate the linear gain coefficient. To characterize the low end of the MGS and HGS dynamic range, additional SIS lamps are also used, with the radiance for each of these lamp levels being calibrated before the start of the thermal vacuum testing campaign. Due to the operation of the DNB, the gains need to be computed for every detector and aggregation mode. An example of the radiance versus digital counts for select aggregation zones is plotted in Figure 4 for all three gain stages. The fits are performed between the specified dynamic range for each gain stage, defined either by L_{min} or the gain transition point on the low end and the gain transition or L_{max} at the high end. For most cases, the relationship between the radiance and dn was well-behaved, similar to J2 and J3 VIIRS. A non-linear behavior was observed in the LGS at low radiance in some aggregation modes. The case of mode 29 resulted in linear fit residuals greater than the uncertainty requirement. Similar behavior was also observed in J2 and J3 VIIRS pre-launch testing and might require some adjustments in the on-orbit calibration to prevent this non-linear behavior from propagating to the MGS or HGS when computing the gain ratios. However, from the on-orbit performance of J2 VIIRS (NOAA-21 after launch), no major impacts due to this behavior have been observed so far, and hence, no modifications have been made to the on-orbit processing. The fit residuals are within the specified calibration uncertainty of 5% at $L_{max}/2$, 10% at the transition from LGS to MGS, 30% at the transition from MGS to HGS, and 100% at L_{min}, except for mode 29 in the LGS. These measurements will be used to create the at-launch tables for LGS gains, offsets, and gain ratios of MGS/LGS and HGS/LGS.

The DNB sensitivity requirement specifies a minimum SNR performance at L_{min}; however, since there was no measurement at L_{min}, a fit is used to evaluate the SNR at L_{min} after adjusting for the spectral differences between the SIS-100 and lunar illumination. In general, all the modes across both HGS CCDS (HGA and HGB) meet or exceed the requirement. The intra-aggregation mode uniformity evaluates the standard deviation of the calibrated radiance for all detectors within the given aggregation mode when viewing a uniform scene. The specification applies to all radiance levels from L_{min} to 0.9 L_{max}, and the limit is either 0.005 *L or half the noise, whichever is larger. In J4, only 13 modes had non-compliances, and those occurred at isolated radiance levels, where the standard deviation was larger than specified. Aggregation mode 29 had the largest fit residuals and issues with uniformity. The inter-aggregation uniformity looks at the difference in the retrieved radiance between the adjacent aggregation modes while viewing a uniform scene. This showed a greater number of non-compliances, which was also observed in previous builds. The HGS showed the best performance with non-compliances found among detectors in only five transitions, as compared to 21 transitions in LGS and 14 in MGS. More details on the JPSS-4 VIIRS DNB can be found here [16].

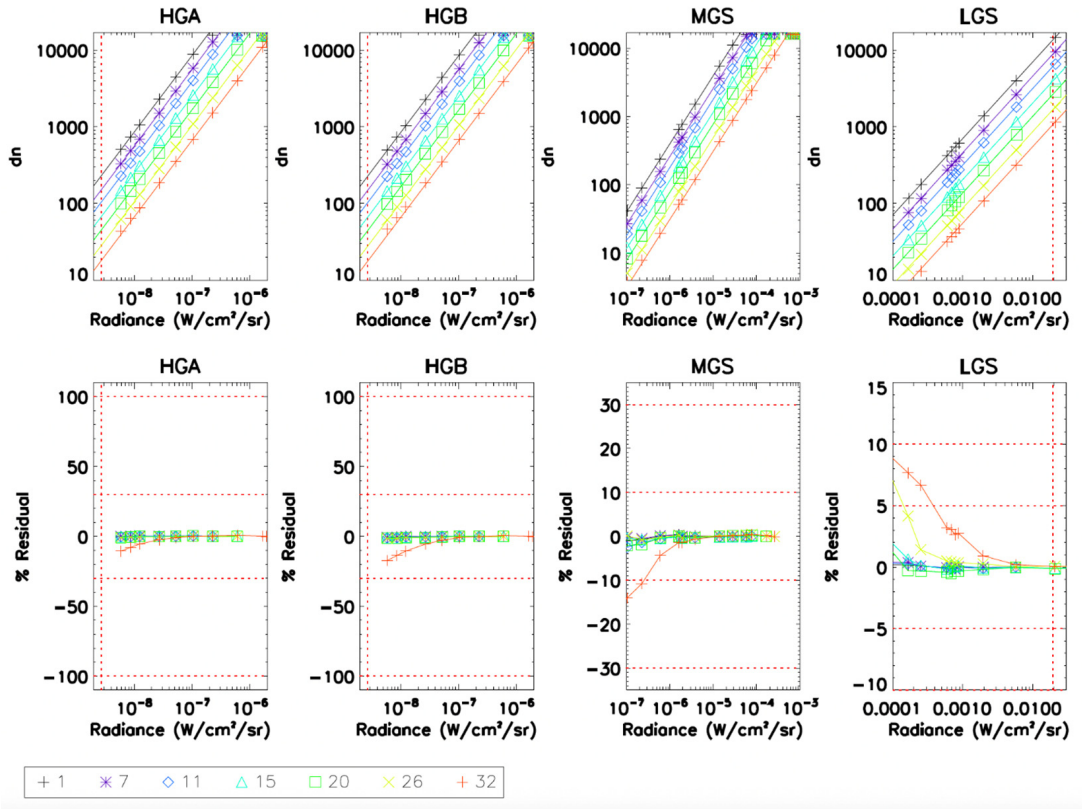


Figure 4. J4 VIIRS DNB response versus radiance for selected aggregation modes.

3.4. Relative Spectral Response Characterization

A high-quality spectral characterization of VIIRS is a prerequisite for deriving the climate quality TOA radiances from Earth observations. This characterization was based on measurements using the SpMA dual monochromator for all bands and the GLAMR laser system for the reflective solar bands. The SpMA and GLAMR measurements for the RSBs were combined to produce a "fused" RSR that was released to the science community and is to be used as a part of the at-launch LUT. For the emissive bands, the SpMA measurements provided the entire characterization. VIIRS has several spectral performance requirements, including center wavelength, bandwidth, 1% limits, and maximum integrated out-of-band (IOOB), which are listed in Table 7, along with the measurements derived by NASA's VIIRS data analysis working group (DAWG) team, which are a part of the released RSR. The measured values are within the prescribed specifications, except for the bandwidth of M14, which has marginal exceedance [8]. Figure 5 shows the released RSR profiles for select bands across all five builds, showing the impact of design/hardware changes through the program, resulting in differences in the RSR profiles for a given band.

Table 7. J4 V2 at-launch RSR metrics compared with the specification. Red fields indicate non-compliance.

Band	Center Wavelength (nm)			Bandwidth (nm)			1 % Limits (nm)				IOOB (%)	
	Meas	Spec		Meas.	Spec		Meas.		Spec		Meas.	Spec
		Center	Tolerance		Bandwidth	Tolerance	Lower Limit	Upper Limit	Lower Limit	Upper Limit		
I1	641.1	640	6	79.2	80	6	594.4	687.7	565	715	0.11	0.5
I2	867.8	865	8	38.5	39	5	835.8	897.8	802	928	0.19	0.7
I3	1612.5	1610	14	63.4	60	9	1547.8	1687.6	1509	1709	0.37	0.7
I4	3754.0	3740	40	379.7	380	30	3485.1	4031.5	3340	4140	0.17	0.5
I5	11,527.5	11,450	125	1838.4	1900	100	10,438.3	12,732.5	9900	12,900	0.09	0.4

Table 7. *Cont.*

Band	Center Wavelength (nm)			Bandwidth (nm)			1 % Limits (nm)				IOOB (%)	
	Meas	Spec		Meas.	Spec		Meas.		Spec		Meas.	Spec
		Center	Tolerance		Bandwidth	Tolerance	Lower Limit	Upper Limit	Lower Limit	Upper Limit		
M1	410.2	412	2	21.3	20	2	397.3	423.7	376	444	0.13	1.0
M2	444.9	445	3	17.0	18	2	434.4	456.5	417	473	0.18	1.0
M3	488.2	488	4	20.1	20	3	475.9	501.2	455	521	0.16	0.7
M4	555.4	555	4	21.2	20	3	541.9	568.8	523	589	0.19	0.7
M5	671.3	672	5	20.7	20	3	651.3	693.6	638	706	0.44	0.7
M6	747.0	746	2	14.8	15	2	736.1	758.2	721	771	0.25	0.8
M7	868.1	865	8	38.5	39	5	836.0	898.0	801	929	0.23	0.7
M8	1241.1	1240	5	20.5	20	4	1225.3	1255.8	1205	1275	0.19	0.8
M9	1381.9	1378	4	15.1	15	3	1368.9	1398.0	1351	1405	0.34	1.0
M10	1612.9	1610	14	63.9	60	9	1548.1	1688.3	1509	1709	0.37	0.7
M11	2252.9	2250	13	47.9	50	6	2207.8	2295.6	2167	2333	0.28	1.0
M12	3685.6	3700	32	192.4	180	20	3527.3	3868.7	3410	3990	0.31	1.1
M13	4024.7	4050	34	155.0	155	20	3870.3	4179.2	3790	4310	0.35	1.3
M14	8564.7	8550	70	345.9	300	40	8233.0	8904.2	8050	9050	0.35	0.9
M15	10,666.5	10,763	113	951.6	1000	100	10,019.0	11,346.3	9700	11,740	0.18	0.4
M16A	11,934.9	12,013	88	964.5	950	50	11,277.1	12,673.5	11,060	13,050	0.19	0.4
M16B	11,935.9	12,013	88	963.7	950	50	11,278.6	12,672.1	11,060	13,050	0.19	0.4
DNBMGS	697.2	700	14	397.5	400	20	490.4	920.7	470	960	0.02	0.1
DNBLGS	692.6	700	14	396.9	400	20	484.5	923.3	470	960	0.10	0.1

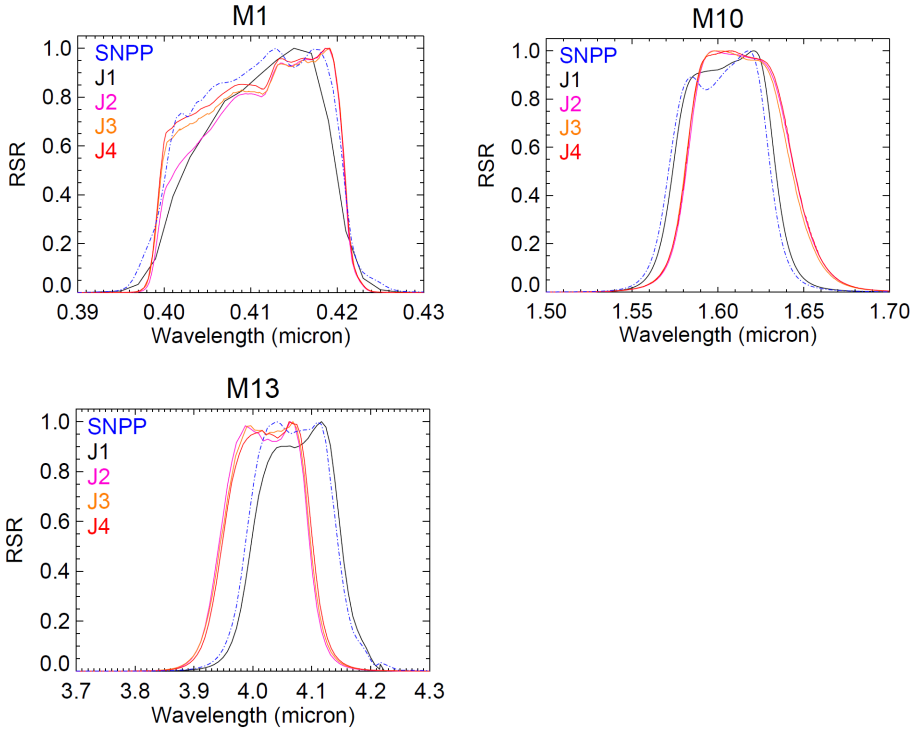


Figure 5. In-band RSR comparison across the different VIIRS builds for select bands.

3.5. Polarization Characterization

The ocean color community uses the calibrated SDRs from bands M1 to M7 (0.41 µm to 0.865 µm) for a variety of ocean color products that require an accurate characterization of the polarization sensitivity to compensate for polarized upwelling Rayleigh scattering. The VIIRS polarization sensitivity requirements for these bands are as follows: maximum amplitude for ±45° scan angle should be within 3% for bands M1, M7, and I2, within 2% for

the rest of the bands, and less than 0.5% uncertainty for all the bands above. The pre-launch test source also uses a 100 cm SIS with a rotating polarizer sheet placed between the source and the sensor, which is rotated in 15° intervals through a full 360° rotation. The sensor response variation with each polarizer sheet rotation is used to characterize the polarization sensitivity of its optical system. A more detailed description of the testing and analysis methodology can be found here [17]. Significant differences have been observed in the polarization sensitivity among the different VIIRS builds, with J1 VIIRS showing the largest sensitivity. Subsequent hardware modifications have reduced the measured polarization sensitivity of the J2-J4 VIIRS. The amplitude of polarization sensitivity or degree of linear polarization (DoLP) is shown for JPSS-4 in Figure 6, with detectors for each band plotted horizontally with increasing detector numbers. The results at different scan angles are shown with different colors and symbols. As seen from the figure, all detectors and scan angles meet the sensor design specification, which is expected based on the results from the previous builds.

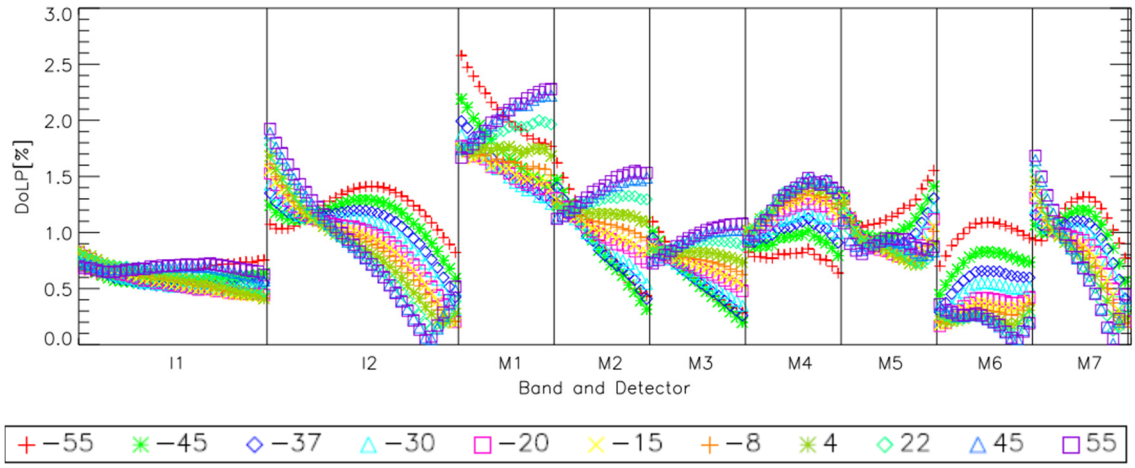


Figure 6. J4 VIIRS degree of linear polarization per band and detector across scan angles (symbols and colors).

3.6. Stray Light Characterization

The far-field stray light performance was characterized using a 1000 W studio lamp placed at several positions to simulate the light from the Earth disk as seen from VIIRS on-orbit, while the telescope was staring at a blackbody. The response for all the lamp positions was summed, weighted by the section of the Earth disk each measurement represents, and scaled from the lamp irradiance to the expected Earth irradiance. The expected counts resulting from stray light are shown in Table 8 for each band. Also presented in Table 8 is the ratio of the dn_{stray} to the dn_{spec}, where the specification is the allowed counts due to stray light, and a value less than unity indicates compliance with the requirement. Results from previous VIIRS builds, now on-orbit, are also included here. Overall, all bands are compliant with the specification for J4 VIIRS, a feature also seen across previous VIIRS builds. The band M11, a non-compliant band in SNPP, was found to be compliant in latter builds because the L_{typ} requirement was changed from 0.12 (SNPP) to 1.0 $W/m^2/sr/\mu m$. Additional details about the stray light methodology and performance can be found in [18]. Separate pre-launch tests were performed to identify and mitigate paths of DNB stray light starting with J2 VIIRS, after significant evidence of stray light was found for SNPP and J1 VIIRS DNB on-orbit in the HGS for observations near the terminator. J2 VIIRS DNB also introduced additional baffling to its design to reduce the impact of stray light, with similar design improvements also implemented in J4 VIIRS.

Table 8. Summary of the J4 VIIRS stray light performance and the ratio of measured stray light to requirement. Comparison with previous VIIRS builds is also shown in the table. Eearth is the Earth's irradiance and has units of watts per meter squared ($W \cdot m^{-2}$). Ltyp is the typical radiance and has units of watts per meter squared per steradian per micrometer ($W \cdot m^{-2} \cdot sr^{-1} \cdot \mu m^{-1}$).

Band	E_{Earth}	L_{typ}	SNPP		JPSS-1		JPSS-2		JPSS-3		JPSS-4	
			dn	L/Spec	dn	L/Spec	dn	L/Spec	dn	L/Spec	dn	L/Spec
M1	1444.10	44.90	2.58	0.15	2.42	0.31	2.23	0.28	4.15	0.45	4.17	0.45
M2	1526.10	40.00	2.53	0.27	2.68	0.30	1.83	0.20	2.65	0.29	3.10	0.35
M3	1563.50	32.00	2.56	0.29	2.89	0.36	1.84	0.19	2.20	0.22	2.68	0.29
M4	1510.70	21.00	2.39	0.32	2.96	0.39	1.58	0.20	2.10	0.25	2.49	0.32
M5	1265.70	10.00	2.38	0.47	2.57	0.55	1.43	0.31	1.38	0.27	2.32	0.50
M6	1088.90	9.60	3.62	0.45	2.95	0.41	2.25	0.32	2.61	0.34	3.27	0.45
M7	833.20	6.40	4.06	0.59	3.29	0.52	3.19	0.50	4.09	0.60	3.95	0.62
M8	353.00	5.40	0.77	0.53	0.44	0.24	0.49	0.37	0.54	0.47	0.28	0.26
M9	262.90	6.00	0.92	0.38	0.36	0.15	0.59	0.33	0.57	0.24	0.33	0.16
M10	165.70	7.30	1.30	0.36	0.22	0.06	0.28	0.10	0.30	0.11	0.16	0.06
M11	56.40	1.00	0.42	3.77	0.09	0.08	0.15	0.13	0.13	0.11	0.11	0.11
I1	1341.30	22.00	0.26	0.26	0.31	0.33	0.32	0.33	0.49	0.51	0.37	0.40
I2	833.20	25.00	0.39	0.15	0.31	0.15	0.36	0.16	0.48	0.23	0.44	0.20
I3	165.70	7.30	0.79	0.25	0.24	0.06	0.27	0.09	0.24	0.09	0.17	0.06

3.7. Near-Field Response Characterization

The near-field response, defined as scattered light within 4° from the RTA line of sight, was characterized using a scatter measurement assembly (ScMA) consisting of a high-energy tungsten filament source for the RSB and a heated ceramic glowbar source for the TEB. The source is collimated before passing through a slit slightly smaller than the width of one M-band detector. Bandpass filters were used to minimize the crosstalk contamination and neutral density filters were used to measure the unsaturated response of the slit and scale it with the near-field measurements made without the ND filters. These two measurements together provide the total NFR with the requirement defined as a structured scene performance specified as the maximum allowable response at a specified angle limit coming off a 20 × 20 km bright target for each band. To estimate the structured scene response, a Harvey-Shack BRDF scattering model was used to fit the measured NFR profile and remove test artifacts and noisy samples. The NFR profiles were convolved to simulate the bright target as described in the sensor-structured scene requirement. Figure 7 shows the normalized response for band M3 detector 8 and represents a typical profile observed in the VIIRS NFR measurements when the sensor is scanning the source through a vertical slit reticle. The figure shows the NFR falling off rapidly from the peak, with the additional sharp drops seen at the field baffle locations.

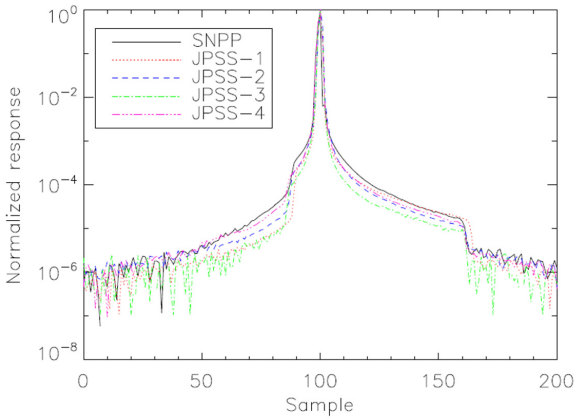


Figure 7. NFR results for band M3 detector 8.

Some minor non-compliances were observed for bands M7, M13, M16A, and I3 in J4 (also in J3 VIIRS) as seen in Table 9. Additionally, bands M8 and M10 also showed non-compliance in J4 NFR testing. As in previous builds, these non-compliances are not expected to show any major impact on science data [19].

Table 9. NFR performance relative to sensor specifications for all builds against the J4 specification. L expressed in W/m^2 sr μm.

Band	Center Wavelength	Angular Separation (mrad)	Lbright	Lspec	SNPP Lscat	J1 Lscat	J2 Lscat	J3 Lscat	J4 Lscat
M1	412	6	162	3.83×10^{-3}	1.08×10^{-3}	1.73×10^{-3}	1.30×10^{-3}	4.60×10^{-4}	3.26×10^{-4}
M2	445	6	180	2.86×10^{-3}	9.99×10^{-4}	1.66×10^{-3}	1.32×10^{-3}	6.29×10^{-4}	2.32×10^{-4}
M3	488	6	160	3.33×10^{-3}	1.00×10^{-3}	1.20×10^{-3}	1.43×10^{-3}	5.33×10^{-4}	3.06×10^{-4}
M4	555	6	160	2.25×10^{-3}	6.16×10^{-4}	1.08×10^{-3}	1.24×10^{-3}	3.83×10^{-4}	1.01×10^{-4}
M5	672	6	115	9.52×10^{-4}	5.48×10^{-4}	6.40×10^{-4}	6.38×10^{-4}	1.81×10^{-4}	3.90×10^{-5}
M6	746	12	147	1.40×10^{-3}	1.57×10^{-4}	1.40×10^{-4}	2.80×10^{-4}	5.60E-05	1.68×10^{-5}
M7	865	6	124	5.44×10^{-4}	4.64×10^{-4}	5.50×10^{-4}	3.37×10^{-4}	3.10×10^{-4}	1.52×10^{-5}
M8	1240	6	57	1.05×10^{-3}	5.87×10^{-4}	3.20×10^{-4}	5.99×10^{-4}	2.84×10^{-4}	3.99×10^{-5}
M9	1378	NA	NA	NA	NA	NA	NA	NA	NA
M10	1610	6	86.1	9.26×10^{-4}	6.44×10^{-4}	3.91×10^{-4}	8.70×10^{-4}	3.80×10^{-4}	3.06×10^{-5}
M11	2250	6	1.2	1.11×10^{-3}	4.20×10^{-4}	3.80×10^{-6}	5.22×10^{-4}	4.00×10^{-4}	0.00
M12	3700	3	0.3	2.09×10^{-3}	1.07×10^{-3}	4.16×10^{-4}	1.30×10^{-3}	4.81×10^{-4}	2.09×10^{-6}
M13	4050	3	1.7	3.42×10^{-3}	1.17×10^{-3}	1.48×10^{-3}	1.68×10^{-3}	5.47×10^{-4}	0.00
M14	8550	NA	NA	NA	NA	NA	NA	NA	NA
M15	10,763	3	12.5	3.43×10^{-3}	9.69×10^{-4}	4.42×10^{-3}	1.06×10^{-3}	1.89×10^{-3}	6.86×10^{-6}
M16	12,013	3	11.3	3.85×10^{-3}	9.98×10^{-4}	5.01×10^{-3}	1.85×10^{-3}	2.31×10^{-3}	3.85×10^{-6}

3.8. Crosstalk Characterization

The VIIRS crosstalk characterization was performed as a part of pre-launch testing. Multiple tests were performed aimed at measuring electronic or optical crosstalk between VIIRS bands. Improvements have been made in the VIIRS design over the JPSS program including updates to detector design and procurement specifications for optical filters. Generally, each successive VIIRS instrument has shown improved crosstalk performance. J4 VIIRS showed two instances of unexpected increases in crosstalk compared to J3. Band M6 detectors show a stronger crosstalk response from bands I2 and M7. Figure 8 presents the response from band M6 detectors, while a single band M7 detector is illuminated during crosstalk testing for J1 through J4 VIIRS instruments. The sender signal in band M7 was measured at about 60% of the dynamic range and scaled to L_{max} for comparison against design requirements. The values displayed in Figure 8 are after scaling to L_{max} and should simulate the same illumination conditions on the sender band. M6 detector responses are shown as a fraction of L_{typ}. The response pattern observed for J4 VIIRS has been seen in past builds, where the along-scan aligned detector measures a larger signal than other detectors, and the following detector measures a negative signal. The magnitude of these responses is much larger (over 3x) than seen previously and is representative of all other measured detectors for these bands. Band I2 detectors induce a similar larger response in the along-scan aligned M6 detectors for J4 VIIRS. The second instance of unexpected crosstalk occurs for band I3, where a strong signal in a single detector causes a larger-than-expected response three detectors away in the same band (band I3) [20].

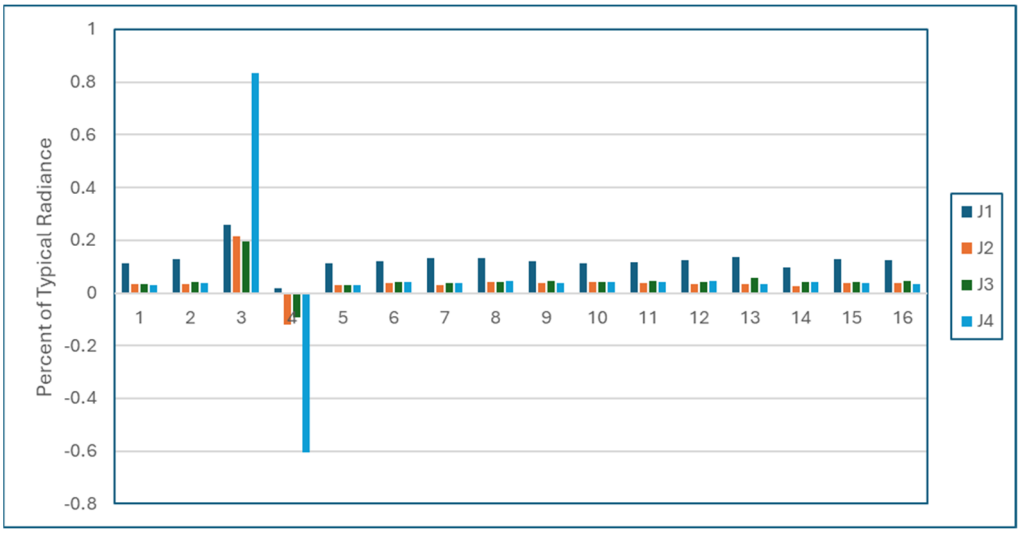


Figure 8. JPSS-4 crosstalk performance for band M6 and comparison with previous builds.

3.9. RVS Characterization

The RVS characterization, also a requirement for the at-launch tables, was performed during the ambient phase of testing for the RSB using the SIS-100 and the Lab Ambient Blackbody (LABB) and onboard BB for the TEB. Data was collected at multiple angles of incidence (AOI) and fitted using a quadratic polynomial after correcting for source drift and background radiances. Figure 9 shows the band-averaged RVS functions for HAM-side A, with minor differences in HAM-B. Except for band M1, the RVS variation for the VIS/NIR bands is less than 0.5%. The SMIR band RVS showed very little variation across the scan angle range of less than 0.5%. In contrast, the LWIR RVS changes up to 10% for band M14 over the range of AOI. All the RSBs and TEBs met their uncertainty specification of 0.3% and 0.2%, respectively, by a significant margin. Overall, the RVS performance observed in J4 VIIRS is very similar to the previous builds and is expected to exhibit similar stable behavior on-orbit, as has been observed in the case of SNPP, JPSS-1, and J2 VIIRS [21].

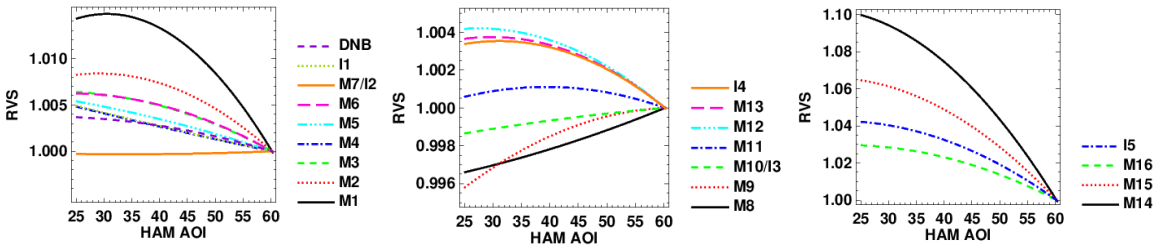


Figure 9. Band-averaged RVS functions for HAM-A of JPSS-4 bands.

3.10. OBC Characterization

In addition to the several functional and system-level tests described above, a comprehensive characterization of the onboard calibrators is also performed. The characterization of the SD and SDSM is of particular importance as the RSB and DNB rely on their observations, with both views using attenuation screens. The SD bidirectional reflectance distribution function (BRDF) and the SD and SDSM solar attenuation screen functions were also characterized by the instrument vendor at the component level. The significant OOB response observed at short wavelengths in the SDSM detectors of J1 VIIRS was addressed using hardware modifications in J2 VIIRS; however, a different source of OOB signal was identified, causing higher uncertainty. Subsequently, these issues were addressed in J3 and carried over to J4 VIIRS.

The SD's BRDF characterization has a particular relevance towards the on-orbit calibration of the VIIRS RSB. The absolute scale of the VIIRS RSB calibration is set using the BRDF measurements acquired pre-launch and is often critical in establishing the calibration consistency between different VIIRS builds. Work is underway to assess the impacts of pre-launch BRDF measurements, possibly assessing the calibration biases between different VIIRS instruments.

The OBC-BB, set to 292 K for most of the TV testing, has six thermistors to monitor the uniformity across the surface. The standard deviation of the six thermistor readings was used to monitor the uniformity and stability change as a function of VIIRS optical temperature, as shown in Figure 10. The OBCBB design requirement is for less than 30 mK of uniformity over the mission lifetime and plays an important role in maintaining the radiometric accuracy of science products. The OBCBB nonuniformity observed in Figure 10 is expected to have an additional increase from the day–night cycling observed on-orbit. While SNPP, J1, and J4 are seen to meet the 30 mK requirement, non-compliances are observed in the case of J2 and J3 VIIRS that could potentially lead to biases in the TEBs based on the satellite position on-orbit. The larger nonuniformity in the J2 was investigated by the instrument vendor and was attributed to the bonding of the heater to the back of the blackbody.

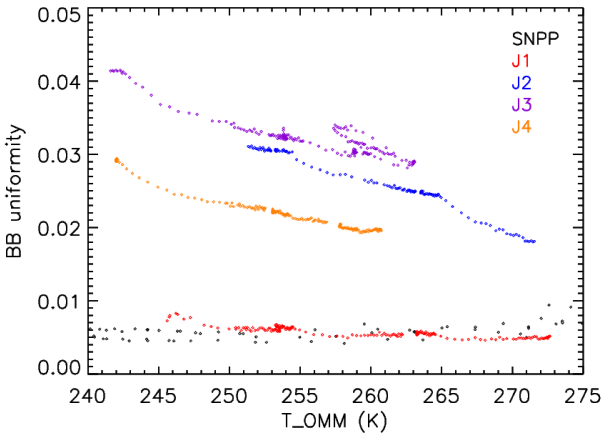


Figure 10. The standard deviation of the six thermistors in the on-board blackbody (OBCBB) in K plotted versus instrument temperature for each JPSS instrument build.

4. Conclusions

The J4 VIIRS instrument underwent a comprehensive pre-launch testing program at the vendor facility in El Segundo, CA, from 2021–2023. Key performance metrics were characterized in terms of comparisons to the design specifications. Key radiometric and spectral performances were discussed in this paper. The J4 VIIRS's performance, as summarized in this work, has met or exceeded its design requirements, with a few exceptions, and is comparable in performance to its predecessor's instruments. The J4 VIIRS spectral band calibration and characterization have shown very good performance in terms of SNR, NEdT, dynamic range, gain transition, and linearity. Some non-linear behavior in the offset coefficient of the calibration equation was observed in the detectors of I3, similar to what was observed in J1 VIIRS. A known mitigation of this issue is available for this behavior, which is expected to diminish any impact on the SDR or environmental data record. Apart from minor non-compliances, the TEB and DNB characterization also met the requirements, showing performance that was comparable to previous builds. The RSR characterization measurements and the subsequent efforts to release the Government Team's at-launch RSR have also been completed. Similar to previous JPSS VIIRS missions, the RSR release is a combination of the GLAMR- and SpMA-based measurements.

In conclusion, the J4 VIIRS test program was completed successfully and provided a comprehensive test data set for sensor requirement verification, with many lessons learned for future Earth-observing sensors. It also showed that the overall pre-launch sensor radiometric performance was of high quality. Efforts are underway to integrate VIIRS to the J4 spacecraft, along with other instruments, and continue the observatory-level testing before launch in 2027.

Author Contributions: Conceptualization, A.A., D.M., J.M. and X.X.; methodology, A.A., D.M., J.M., T.S. and D.L.; software, A.A., D.M., J.M., T.S. and D.L.; validation, Q.J. and C.S.; formal analysis, A.A.; investigation, A.A.; resources, X.X.; data curation, A.A.; writing—original draft preparation, A.A.; writing—review and editing, all.; visualization, A.A.; supervision, X.X.; project administration, X.X.; funding acquisition, X.X. All authors have read and agreed to the published version of the manuscript.

Funding: This work received no external funding.

Data Availability Statement: The original contributions presented in this study are included in the article. Further inquiries can be directed to the corresponding author.

Acknowledgments: Raytheon Technologies for design, execution, and data dissemination for the preflight characterization of the JPSS-4 VIIRS instrument. James McCarthy and Jason Geis for their efforts as a part of NASA's onsite team. The efforts of Chris Moeller for leading the RSR characterization effort are also acknowledged and appreciated.

Conflicts of Interest: Authors Amit Angal, Daniel Link, Thomas Schwarting, Jeff McIntire and Qiang Ji were employed by the company Science Systems and Applications Inc. Author David Moyer was employed by the company The Aerospace Corporation. Author Chengbo Sun was employed by the company Global Science & Technology, Inc. The remaining author declares that the research was conducted in the absence of any commercial or financial relationships that could be construed as a potential conflict of interest.

References

1. Zhou, L.; Divakarla, M.; Liu, X. An Overview of the Joint Polar Satellite System (JPSS) science data product calibration and validation. *Remote Sens.* **2016**, *8*, 139. [CrossRef]
2. Welsch, C.; Swenson, H.; Cota, S.A.; DeLuccia, F.; Haas, J.M.; Schueler, C.; Durham, R.M.; Clement, J.E.; Ardanuy, P.E. VIIRS (Visible Infrared Imager Radiometer Suite): A Next-Generation Operational Environmental Sensor for NPOESS. In Proceedings of the IEEE 2001 International Geoscience and Remote Sensing Symposium (IGARSS), Sydney, Australia, 9–13 July 2001. [CrossRef]
3. Rogers, M.A.; Miller, S.D.; Seaman, C.J.; Torres, J.; Hillger, D.; Szoke, E.; Line, W.E. VIIRS after 10 Years—A Perspective on Benefits to Forecasters and End-Users. *Remote Sens.* **2023**, *15*, 976. [CrossRef]
4. Cao, C.; Xiong, J.; Blonski, S.; Liu, Q.; Uprety, S.; Shao, X.; Bai, Y.; Weng, F. Suomi NPP VIIRS sensor data record verification, validation, and long-term performance monitoring. *J. Geophys. Res. Atmos.* **2013**, *118*, 11664–11678. [CrossRef]
5. Sun, J.; Wang, M. VIIRS reflective solar bands calibration progress and its impact on ocean color products. *Remote Sens.* **2016**, *8*, 194. [CrossRef]
6. Wang, W.; Cao, C.; Blonski, S. NOAA-21 VIIRS Thermal Emissive Bands Early On-Orbit Calibration Performance and Improvements. *IEEE Trans. Geosci. Remote Sens.* **2024**, *62*, 5006313. [CrossRef]
7. Oudrari, H.; McIntire, J.; Xiong, X.; Butler, J.; Lee, S.; Lei, N.; Schwarting, T.; Sun, J. Prelaunch radiometric characterization and calibration of the S-NPP VIIRS sensor. *IEEE Trans. Geosci. Remote Sens.* **2014**, *53*, 2195–2210. [CrossRef]
8. Oudrari, H.; McIntire, J.; Xiong, X.; Butler, J.; Ji, Q.; Schwarting, T.; Lee, S.; Efremova, B. JPSS-1 VIIRS radiometric characterization and calibration based on pre-launch testing. *Remote Sens.* **2016**, *8*, 41. [CrossRef]
9. Oudrari, H.; McIntire, J.; Xiong, X.; Butler, J.; Ji, Q.; Schwarting, T.; Angal, A. An overall assessment of JPSS-2 VIIRS radiometric performance based on pre-launch testing. *Remote Sens.* **2018**, *10*, 1921. [CrossRef]
10. McIntire, J.; Xiong, X.; Butler, J.J.; Angal, A.; Moyer, D.; Ji, Q.; Schwarting, T.; Link, D.; Sun, C. An overall assessment of JPSS-3 VIIRS radiometric performance based on pre-launch testing. *Remote Sens.* **2022**, *14*, 1999. [CrossRef]
11. Wang, Z.; Barsi, J.; Thome, K.; Wenny, B.N.; McAndrew, B.; Efremova, B.; McCorkel, J. Uncertainty budget for detector-based absolute radiometric calibration with GLAMR. *Appl. Opt.* **2024**, *63*, 3015–3028. [CrossRef] [PubMed]
12. Moeller, C.; Schwarting, T.; Moyer, D.; Barsi, J.; Angal, A. The JPSS-4 VIIRS version 2 (at-launch) relative spectral response characterization. *Earth Obs. Syst. XXIX* **2024**, *13143*, 1314315.

13. Moyer, D.; Angal, A.; Oudrari, H.; Haas, E.; Ji, Q.; De Luccia, F.; Xiong, X. JPSS-1 VIIRS prelaunch reflective solar band testing and performance. *Remote Sens.* **2022**, *14*, 5113. [CrossRef]
14. Angal, A.; Moyer, D.; Xiong, X.; Ji, Q.; Link, D. Pre-Launch Reflective Solar Band Radiometric Performance for JPSS-3 and -4 VIIRS. *Remote Sens.* **2024**, *16*, 4799. [CrossRef]
15. Moyer, D.; Angal, A.; McIntire, J.; Xiong, X. Pre-Launch Thermal Emissive Band Radiometric Performance for JPSS-3 and -4 VIIRS. *Remote Sens.* **2024**, *16*, 4630. [CrossRef]
16. Link, D.; Schwarting, T.; Angal, A.; Xiong, X. Pre-Launch Day-Night Band Radiometric Performance of JPSS-3 and -4 VIIRS. *Remote Sens.* **2025**, *17*, 1111. [CrossRef]
17. Moyer, D.; McIntire, J.; Angal, A.; Xiong, X. Pre-Launch Polarization Assessment of JPSS-3 and-4 VIIRS VNIR Bands and Comparison with Previous Builds. *Remote Sens.* **2024**, *16*, 2178. [CrossRef]
18. Ji, Q.; McIntire, J.; Link, D.; Xiong, X. Pre-launch characterization of VIIRS straylight. *Earth Obs. Syst. XXVII* **2022**, *12232*, 122321B.
19. Link, D.; Schwarting, T.; Angal, A.; Xiong, X. Assessment of the pre-launch JPSS-4 VIIRS near-field response in an ambient environment. *Earth Obs. Syst. XXVII* **2022**, *12232*, 1223203.
20. Link, D.; Ji, Q.; Schwarting, T.; Angal, A.; Xiong, X. Prelaunch characterization of JPSS VIIRS crosstalk. *Earth Obs. Syst. XXIX* **2024**, *13143*, 131430E.
21. McIntire, J.; Moyer, D.; Angal, A.; Xiong, X. JPSS-3/4 VIIRS response versus scan angle characterization and performance. *Front. Remote Sens.* **2023**, *4*, 1303347. [CrossRef]

Disclaimer/Publisher's Note: The statements, opinions and data contained in all publications are solely those of the individual author(s) and contributor(s) and not of MDPI and/or the editor(s). MDPI and/or the editor(s) disclaim responsibility for any injury to people or property resulting from any ideas, methods, instructions or products referred to in the content.